TU DELFT

BACHELOR THESIS

PERFORMED AT FACULTY OF APPLIED SCIENCES AT THE DELFT UNIVERSITY OF TECHNOLOGY

Modelling the extraction efficiency inside a Molten Salt Reactor

Author
T. STRIEKWOLD
4384318

Supervisor
Dr. E. CAPELLI
F. ALSAYYARI
Thesis Comittee
Prof. Dr. Ir. J.L. KLOOSTERMAN
Dr. Z. PERKÓ

Date of Defence: 04-09-2018

Abstract

The world's energy consumption is rapidly increasing and with the corresponding growth in emission of greenhouse gases, a new sustainable way of energy production is needed. Therefore a Molten Salt Reactor (MSR) fuelled with thorium is introduced. The MSR is a generation IV reactors which is low in risk and can be fuelled with abundant thorium instead of uranium.

Inside a MSR, fission products like noble gasses and metals need to be extracted. The noble metals xenon and krypton are neutron poisons and therefore decrease the reaction activity. Additionally, metallic particles plate out on metal surfaces which causes damage to the reactor. To extract noble gasses helium bubbling is used. With helium bubbling, hydrophobic particles attach to the gas bubbles which makes it possible to collect the particles. This process is called flotation. Since flotation is a process depending on several correlated variables, it is hard to predict the extraction efficiency from physical calculations. Since measurements are very time-consuming, a model is desired to predict the extraction efficiency. To make this model, a combination of Proper Orthogonal Decomposition and Radial Basis Function is applied. It is in the aim of this research to see if a reduced model can be made to predict the extraction efficiency.

Using a set-up pre-examined by Journee [1], a time dependent extraction efficiency model is trained by doing measurements with different flow rates $\dot{V}$, particles sizes R and particle densities ρ. A time dependent extraction for molybdenum and iron is found, from which only molybdenum turned out to be satisfactory as a result of shortage of data for iron. The model on molybdenum was able to make an approximation that had only 8% relative error with the measurement, but also consisted of a prediction with an error of 61%. Therefore it can be concluded that more experiments need to be done to see if the reduced model is appropriate.

In further research more experiments should be done for at least iron and other particles with different densities. This should be done with the same flow rate and particle sizes as used for molybdenum. The set-up should be improved to make sure all samples have the same volume.

Contents

Chapter 1

Introduction

1.1 Nuclear Energy

With the growth in global populations, the energy consumption increases. According to the U.S Energy Information Administration (EIA) [2], the global energy consumption will have grown with 28% between 2015 and 2040. Nuclear energy is the second fastest growing producer of this valued energy. EIA expects an average of 1.5% increase of nuclear energy production per year. Nuclear energy will therefore become more important on the energy consumption scale. With its importance growing, it is time to look for safer and more sustainable ways of nuclear energy.

1.2 Thorium Fuel Cycle

For many years thorium has been a prospecting outcome in the nuclear world. Unfortunately most thorium related projects were stopped because of cost and proliferation concerns or technological problems [3]. Uranium was chosen as the fuel for most reactors instead. With growing concerns about the long-term availability of cheap uranium, new research is conducted to see if there is a future for thorium as a fuel.

The major isotope of thorium in nature is thorium-232. Unlike uranium which is a fissile element, thorium-232 is fertile [4]. Therefore thorium needs uranium or plutonium to start a reaction. Thorium-232 will absorb a neutron from the fission of uranium or plutonium and thorium-233 is produced. Thorium-233 will decay to uranium-233 via protactinium-233, which in turn decays while producing neutrons. These neutrons are again captured by thorium-233 and this way the reaction is sustained [5]. This cycle is displayed in figure 1.1.

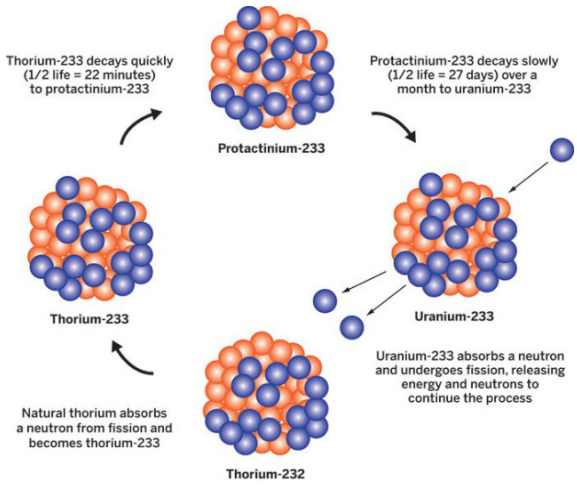

Figure 1.1: Thorium fuel cycle: the U-233 fission produces neutron, neutrons are absorbed by Th-232 and produce Th-233, Th-233 decays and forms Pa-233. U-233 is formed after Pa-233 decays and produces new neutrons when decaying. These neutrons are again used to produce Th-233 out of Th-232 [6]

.

The benefits of thorium are listed below:

- thorium is more abundant than uranium [7, 8].
- low amount of transuranics produced and has a low radio-toxicity at long term.
- low amount of weapons produced plutonium as a fission product of Thorium [9].
- theoretical lower cost compared with uranium fuel cycle because there is no enrichment needed.

1.3 Molten Salt Reactor

The Molten Salt Reactor (MSR) was initially designed for the use of nuclear propulsion programs for aircrafts. Here a MSR was interesting because of its high power density. Though the experiment was successful it was cancelled because it became clear in-air refuelling was possible [10]. When the necessity for a MSR in the aircraft industry was gone , the reactor was further developed as a new breeder reactor [11].The MSR is a generation IV reactor which has a liquid as fuel instead of solid fuel rods. The high potential of liquid-fuel reactor comes from the following beneficial characteristics relative to the solid-fuel reactor:

- Since the fuel is liquid it expands when heated, which slows down the nuclear reactions, thus making the reactor self-regulated. This is caused by the negative temperature feedback coefficient.[12].
- The MSR also has a negative void feedback coefficient. This also causes a self-regulated behaviour [13].
- A MSR has the ability to use continuous fission-product removal. This way fission products and actinides can be extracted. Extracted actinides can then be reintroduced into the fuel circuit. [12].

- The MSR is designed such that if the molten salt is overheated, freeze-plugs at the bottom of the reactor will melt and all the fuel salt will drain into passively cooled critically safe dump tanks. Therefore overheating is made impossible[10].
- MSR does not operate under high pressure and does not need water as a coolant. This makes a steam explosion impossible[12].

1.3.1 General description of the MSR

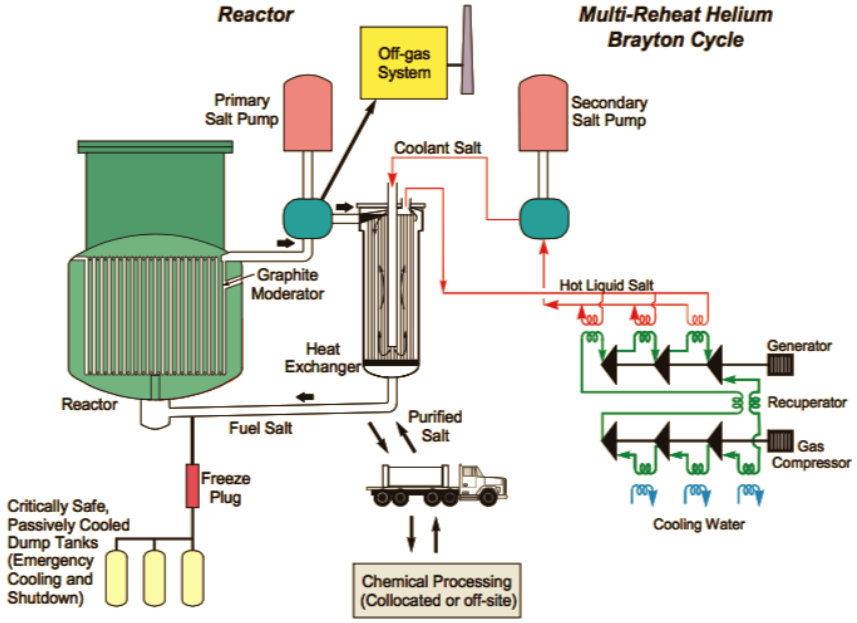

Figure 1.2: Generation IV MSR with multi-reheat helium Brayton cycle[11]

In a Molten Salt Reactor, as displayed in figure 1.2, a molten fluoride salt with dissolved fuel flows into a reactor core. Here fission reactions take place within the fuel salt. After flowing through the reactor core, the fuel salt reaches the primary heat exchanger. The heat is transferred from the fuel salt to a secondary molten salt coolant. The secondary molten salt coolant transfers the heat to the Brayton cycle to produce electricity or a hydrogen production facility.

1.3.2 Fission Products

As the fission activity of thorium is depending on the available neutrons, it is important to remove elements that can also absorb free neutrons. Noble gases like xenon and krypton should therefore be removed to prevent so called neutron poison [14]. Besides neutron poison, noble metals tend to form metallic particles, which can plate out on the metal surfaces of the reactor which can cause damage[11]. These noble metals should therefore also be extracted from the molten salt. The properties of some noble gasses and metals are displayed in table 1.1 and 1.2. The liquid in the Molten Salt Reactor is a composition of $LiF - BeF_2 - ThF_4 (70\% - 18\% - 12\%)$, which forms a molten salt. Its properties are displayed table 1.3.

Name	Symbol	Atomic number	Density(g/cm^3)
Xenon	Xe	54	$5.9 * 10^{-3}$
Krypton	Kr	36	$3.73 * 10^{-3}$

Table 1.1: Noble gasses present in a Molten Salt Reactor which need to be extracted to prevent neutron poison[15, 16]

Name	Symbol	Atomic number	Density(g/cm^3)
Molybdenum	Mo	42	10.22
Technetium	Tc	43	11
Ruthenium	Ru	44	12.2
Rhodium	Rh	45	12.44
Palladium	Pd	46	12.02

Table 1.2: Metallic particles present in a Molten Salt Reactor which need to be extracted to prevent them from plating out to the inside of the reactor[17, 18]

Name	Density ρ g/cm^3 @ 900°K	Kinematic viscosity ν mm^2/s
Molten Salt [19]	3.098	$1.40 * 10^{-2}$

Table 1.3: properties molten salt

1.4 Research goals

To extract particles out of a Molten Salt Reactor, helium bubbles can be used. The hydrophobic particles will attach to the gas bubbles and will float to the surface. There the particle-bubble aggregate will detach and the particles can be extracted. This process is called flotation. Since flotation is depending on several correlated variables it is very hard to make a physical calculation to predict the total extraction efficiency of flotation. Therefore, a model is needed. Because some variables are correlated, a reduced model is made. This work looks into the possibilities to make a reduced model by varying the variables particle size R, particle density ρ and volumetric gas flow rate $\dot{V}$.

Chapter 2

Flotation process

Flotation is a separation process which can be used to achieve online fission-product removal inside a Molten Salt Reactor. The primary aim in flotation is to attach hydrophobic particles to gas bubbles which will carry the particles to the surface. A froth zone forms where the particles will separate from the bubble and can be collected [20]. The flotation process is depending on several interactions and parameters such as internal forces, particles properties and chemicals used [21]. The forming of a particle-bubble aggregate which is necessary for flotation can be divided into three main steps. These are particle-bubble collision, attachment and detachment. This can be seen from the following formula which describes the probability of a particle being collected by a bubble [22]:

$$P = P_c P_a (1 - P_d) \tag{2.1}$$

in this equation P_a is the probability of attachment, P_d the probability of detachment and P_c is the probability of collision.

Probability of collision

The probability that particles will collide with each other depends on the particle size D_p, bubble size D_b and the flow regime around the bubble. As there is not a single relation between P_c and the ratio D_p/D_b, which describes the whole range of bubble sizes, a general relation is derived:

$$P_c = A\left(\frac{D_p}{D_b}\right)^n \tag{2.2}$$

Where the variables A and n are given for four different flow regimes. Stokes describes the probability of collision for the smallest bubbles ($Re \ll 1$), the second and third equation give variables in the intermediate bubble sizes and the potential limit for the biggest bubbles ($80 < Re < 500$ [23]) [22][24].

Flow conditions	A	n
Stokes	$2/3$	2
Intermediate 1	$3/2 + (4Re^{0.72})/15$	2
Intermediate 2	$\frac{3}{2}\left[1 + \frac{3/16Re}{1+0.249Re^{0.56}}\right]$	2
Potential	3	1

Table 2.1: flow conditions and their variables

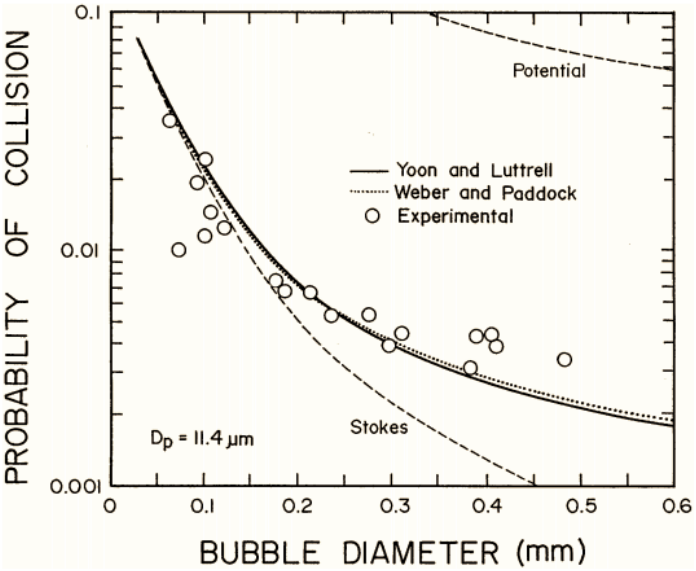

Figure 2.1: Effects of bubble size on collision efficiency under given flow conditions [24]

In figure 2.1 the different flow regimes are plotted according to experiments done by Yoon [24]. It becomes clear that Stokes underestimates the collision probability unless the particles size becomes sufficiently small. The potential approximation overestimates the experimental values. The intermediate approximation, in the figure referred to as 'Yoon and Luttrell' and 'Weber and Paddock', give a good estimate of the outcome.

Probability of Attachment

The probability of attachment is mainly affected by the way the bubbles are distributed and how much the contact area is already covered with particles. Besides, the particles have to be sufficiently hydrophobic to be able to make a strong enough attachment [25]. Both the flowrate and the hydrophobic characteristics of the particles are high enough to make the assumption that the majority of the particles will collide with a bubble and if the time of sliding is long enough the particle will attach.

Probability of Detachment

For small particles P_d is negligible because of its low inertia and considered equal to 0 [24]. When the diameter increases the detachment forces outweigh the attachment forces and therefore the particle detaches from the bubble. The upper grain limit is the size of a particle for which the kinetic energy of the particle to the energy required or particle detachment is reached. The theoretical upper grain size limit of floatability $R_{p,max}$ can be calculated from the following force balance [26, 27]:

$$\begin{aligned}\frac{4}{3}\pi R_{p,max}^3 \rho_p b_m = \frac{2}{3}\pi R_{p,max}^3 \rho_{Fl} g \Bigg[1 - \frac{2\rho_p}{\rho_{Fl}} - cos^3\omega^* + \frac{3h}{2R_{p,max}} sin^2\omega^* - \\ \frac{3}{a^2 R_{p,max}^2} sin\omega^* sin(\omega^* + \theta)\Bigg] - \pi R_{p,max}^2 sin^2\omega^* \left(\frac{2\sigma}{R_B} - 2R_B\rho_{Fl}g\right)\end{aligned} \tag{2.3}$$

Where ρ_p is the density of particles in g/cm^3, b_m is the turbulent acceleration in cm/s^2, $\rho_F l$ is the fluid density in g/cm^3, g the gravitational acceleration in cm/s^2, ω^* the stream function of fluid flow angular frequency in s^{-1}, θ the static contact angle in degrees, R_b the bubble radius in cm and σ the surface tension in mN/m. This equation can be solved numerically or by separatly plotting the kinetic energy and the detaching energy as a function of R_p. Both Schulze and Crawford and Ralston have experimentally shown the applicability of equation 2.3 [27].

Force balance on a particle bubble aggregate

Because of the hydrophobic characteristic of the particles used in this work and considerably low probability of detachment, the aggregate is not very common to detach. However, this does not mean all aggregates are extracted. For particles which are not heavy enough to detach, it could happen that instead of detaching, the whole aggregate sinks to the bottom of the column. Therefore apart from the probabilities on the particle-bubble aggregation, also the net force working on the aggregate should be taken into account.

Chapter 3

Proper Orthogonal Decomposition and Radial Basis Functions

As can be seen in the chapter (2), extraction efficiency is depending on many variables. Because several of these variables are correlated it is very hard to make a physical calculation on the expected extraction efficiency. Therefore, it is hard to make a model from experimental data of the extraction efficiency. Hence, a reduced model has to be derived. This chapter explains how a reduced model is derived for this work.

3.1 Proper Orthogonal Decomposition

To reduce the number of variables Proper Orthogonal Decomposition (POD) can be used. The central idea of POD is to rewrite a high dimensional system of correlated variables into a system with uncorrelated vectors. These new uncorrelated vectores $\boldsymbol{\varphi}_1, \boldsymbol{\varphi}_2, \ldots, \boldsymbol{\varphi}_K$ are called the Principal Components (PC's) and form a new basis of the model. Each PC will be multiplied by amplitudes so that each of the original data sets is described in the following way:

$$\boldsymbol{U} = \boldsymbol{\Phi}\boldsymbol{A} \tag{3.1}$$

Hence when the orthogonal basis $\boldsymbol{\Phi}$ is defined, a matrix $\mathbf{A}$ has to be found where the multiplication between $\boldsymbol{\Phi}$ and $\mathbf{A}$ gives the original system $\mathbf{U}$. The PC's are sorted in such a way that the first PC's have the most information of the original data set, and the last have almost no information. Therefore the last few PC's can be left out without causing significant error. Now, one can rewrite a N-dimensional system into a K-dimensional set of uncorrelated systems where $K < N$, without losing too much information. The truncated system can now be expressed as:

$$\boldsymbol{U} \approx \overline{\boldsymbol{\Phi}}_K \overline{\boldsymbol{A}}_K \tag{3.2}$$

3.1.1 Singular Value Decomposition

As an extension on the previous discussed method to decrease the amount of dimensions in a system and write the system in uncorrelated vectors, the singular value decomposition approach can be used in situations of non-square matrix $\mathbf{U}$. Considering a $N \times M$ matrix $\mathbf{U}$, there exists an orthogonal $N \times N$ matrix $\boldsymbol{V}^1$, and a $M \times M$ matrix $\boldsymbol{V}^2$ such that

$$\boldsymbol{U} = \boldsymbol{V}^1 \boldsymbol{S} (\boldsymbol{V}^2)^T \tag{3.3}$$

here $\mathbf{S}$ is a rectangular $N \times M$ matrix with only nonzero elements on the diagonal equal to

$$s_{ii} = \sigma_i, \sigma_1 > \sigma_2 > \ldots > \sigma_r > 0 \qquad r = min(M, N) \tag{3.4}$$

These diagonal elements σ_i are called singular values of U. They give an indication of how much variation there is in the direction of that Principal Component. Therefore the ordering of the PC's can be found by looking at the value of σ_i. The Principal Components as described in the previous subsection are collected in the matrix $\boldsymbol{V}^1_K$. The reduced system now looks like this:

$$\boldsymbol{U} \approx \overline{\boldsymbol{V}^1}_K \overline{\boldsymbol{A}}_K \tag{3.5}$$

3.2 Radial Basis Function

Collected in matrix $\mathbf{U}$ are different datasets for different inputs (nodes). In order to make an approximation for inputs other than these node, a continuous function over the whole input domain is needed. Radial Basis Functions (RBF's) are used to create this continuous function depending on the entire dataset. The approximation for this radial basis function is a linear combination of g_i, that can be written as a function of non-linear functions, namely

$$f(\boldsymbol{x}) \approx \sum_{j=1}^{N} \alpha_i \cdot g_i(\boldsymbol{x}) \tag{3.6}$$

where α_i are the coefficients of the linear combinations spanned up with nonlinear functions g_i. There are several ways to determine g_i. The most common one is the euclidian distance given by

$$g_i(\boldsymbol{x}) = g(||\boldsymbol{x} - \boldsymbol{x}_i||) \qquad i = 1, 2, \ldots, N \tag{3.7}$$

with g_i well defined, α_i needs to be found to get the final continuous function. This can be done by describing the system as follows

$$\boldsymbol{G} = \begin{bmatrix} g_1(\boldsymbol{x}_1) & \cdots & g_N \\ \vdots & \ddots & \vdots \\ g_1(\boldsymbol{x}_N) & \cdots & g_N(\boldsymbol{x_N}) \end{bmatrix} \tag{3.8}$$

$$\boldsymbol{\alpha} = [\alpha_1, \alpha_2, \ldots, \alpha_n]^T \qquad \boldsymbol{Y} = [y_1, y_2, \ldots, y_N]^T \tag{3.9}$$

$$\boldsymbol{a} \cdot \boldsymbol{G} = \boldsymbol{Y} \tag{3.10}$$

For every data set with outcomes $\mathbf{Y}$ the unknown interpolation coefficients can be derived. When these interpolation coefficients are know, an approximation of the outcome can be given at any given point $\mathbf{x}$. Because the interpolation coefficients are calculated all at the same time and involve all known values of functions, a big advantage is created over normal interpolation techniques. Another advantage is given by the fact that there is no need for an regular distribution of the nodes. This means, the different inputs do not have to be equally spaced to make an approximation. A scattered grid of inputs

though, leads to an increase in error of the interpolation. This error is also influenced by the choice between different RBF [28].

To obtain the most accurate prediction from the radial basis function, the radial basis functions displayed in equations 3.12-3.15 are compared. The script defines a maximal error for the truncated matrix. This is, the model will truncate the system until this max error is reached. The error is defined as the L2-norm between the original and the truncated matrix.

$$Thin-Plate\ splines: \quad ||\mathbf{x}-\mathbf{x}_j||\, ln(||\mathbf{x}-\mathbf{x}_j||) \tag{3.11}$$

$$Linear\ splines: \quad ||\mathbf{x}-\mathbf{x}_j|| \tag{3.12}$$

$$Cubic\ splines: \quad ||\mathbf{x}-\mathbf{x}_j||^3 \tag{3.13}$$

$$Gaussian: \quad exp\left(-\frac{||\mathbf{x}-\mathbf{x}_j||}{c_j^2}\right) \tag{3.14}$$

$$Multiquadric: \quad \sqrt{1+\frac{||\mathbf{x}-\mathbf{x}_j||^2}{c_j^2}} \tag{3.15}$$

3.3 Proper Orthogonal Decomposition & Radial Basis Functions

The purpose of RBF is to find a continuous function depending on input vector $\mathbf{p}$ which describes system outcome $\mathbf{u}$.

$$f(\boldsymbol{p}) = \boldsymbol{u} \tag{3.16}$$

It is also possible to use the RBF on an already truncated system. Since this truncated system is represented in terms of amplitudes $\overline{\boldsymbol{A}}$ it is possible to write equation 3.16 as

$$f(\boldsymbol{p}) = \overline{\phi} \cdot f_a(\boldsymbol{p}) = \boldsymbol{u} \tag{3.17}$$

The same technique used for RBF can be applied to approximate f_a. By multiplying matrix $\overline{\boldsymbol{A}}$ by matrix $\mathbf{G}$, a third matrix is obtained which describes the system as follows:

$$\boldsymbol{u} \approx \overline{\Phi} \cdot \boldsymbol{B} \cdot \boldsymbol{g}(\boldsymbol{p}) \tag{3.18}$$

In equation 3.18 it becomes clear that the originally heavy calculation on a big dataset and interpolation on it, is replaced by one matrix-multiplication. For every following prediction for a random input, only $\boldsymbol{g}(\boldsymbol{x})$ has to be determined, since matrices $\overline{\phi}$ and $\boldsymbol{B}$ are constant and trained for every model. This method is used to make a model and is summarized in figure 3.1.

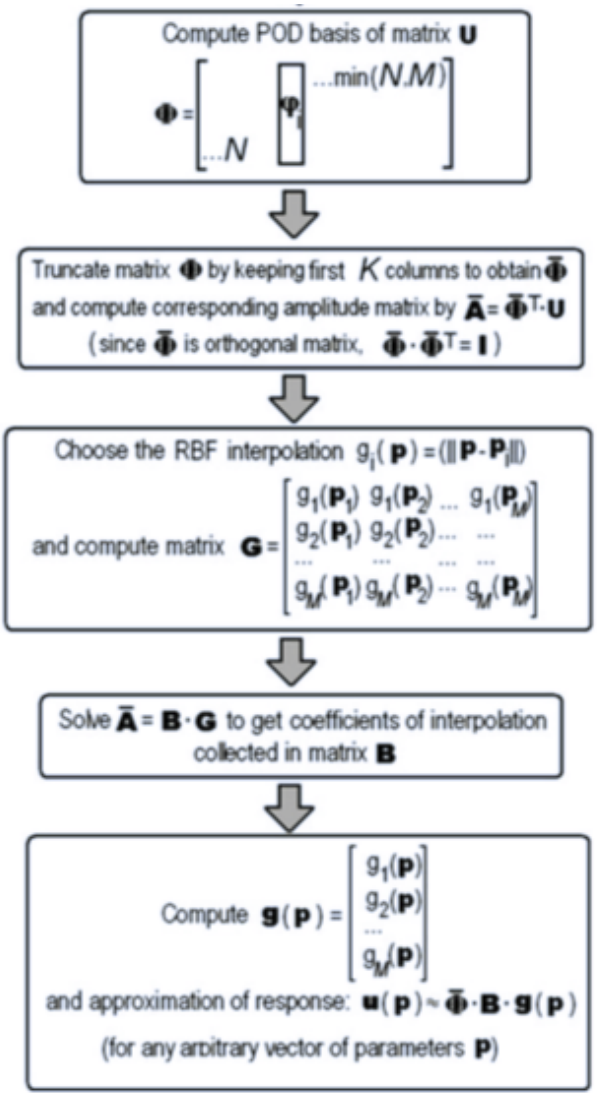

Figure 3.1: Flowchart of the operations needed to be performed in order to train the POD-RBF model. To obtain matrix $\mathbf{\Phi}$, SVD is applied on experimental results compiled into matrix $\mathbf{U}$ [28]

.

Chapter 4

Materials and Methods

4.1 Set-up

Column

The experiments in this work were performed using the set-up displayed in figure 4.1a. The column of the set-up has a length of 50 cm and a inner diameter of 26mm [1]. At the top and bottom of the column there are two tube connections. The top connection is used to insert the particles into the column and the second is to empty the column. The bottom opening is connected to the bubble distributor with a flange connection. The bottom of the column and its details are displayed in figure 4.1b

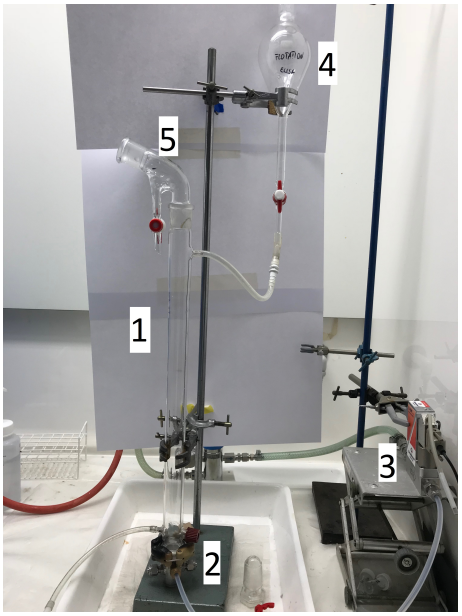

(a) used during experiment with 1: flotation column, 2: sintered metal plate with airflow through it, 3: mass flow meter, 4: Separatory funnel, 5: Hallimond tube

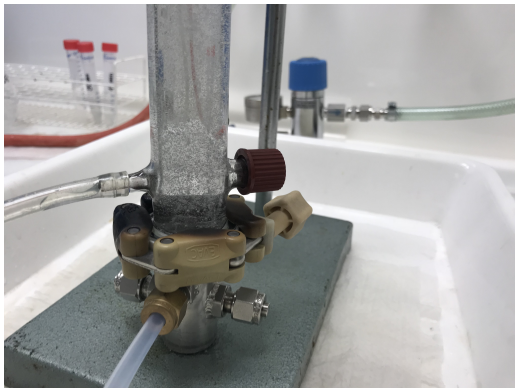

(b) bottom of the column. On the left the tube connection to extract the content of the column can be seen. Also the flange connection to the bubble distributor can be noticed.

Figure 4.1: set-up used (a), bottom connection (b)

Hallimond tube

On top of the column is a modified Hallimond tube attached. The Hallimond tube is equipped with a manual valve to be able to take samples during the extraction experiment. The Hallimond tube has an angle of 115 degrees relative to the column. This angle chosen to prevent the bubbles from colliding with the wall of the tube which causes particles to detach from the bubble. This angle also makes sure that the particles that will detach at the gas-liquid interface, will not flow back into the column. Some particles that do not enter the reservoir will form a deposit layer at the arch of the Hallimond tube. The Hallimond tube and its deposit are displayed in figure 4.2a and figure 4.2b.

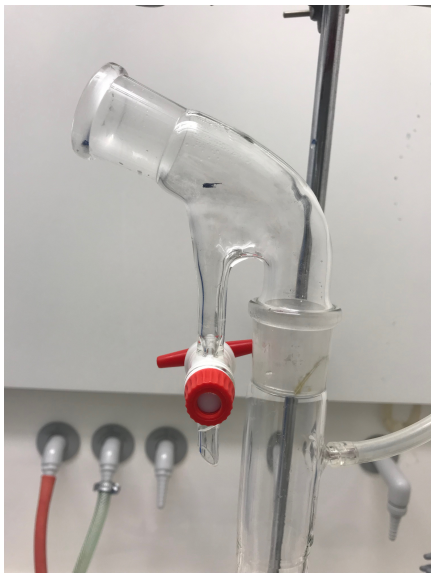

(a) empty Hallimond tube

(b) deposit of extracted particles which are accumulated during the whole experiment but only measured at t=60.

Figure 4.2: hallimond tube (a), hallimond tube with deposit during experiment (b)

Separatory funnel

A separatory funnel is used to insert the particles into the column via the upper tube connection. The particles are inserted by opening the valve of the separatory funnel. By using this valve all particles can be inserted at the same time after the bubbling is started. As a result, it is impossible for the particles to sink to the bottom before the bubbling is started.

Gas Supply

The gas used in the experiment is air. The air supply into the column is controlled by the mass flow meter. The air from the line is reduced to 2 bar by a pressure controller. The pressure meter shows the outlet of the air valve. It is important that the air input from the line is high enough so no pressure drop will occur during the experiment. The air valve is connected to a Bronkhorst gas controller. The eventual gas input is controlled by two software programs: FlowDDE and FlowView. The air is inserted uniformly into the column by a sintered metal plate through which bubbles are formed.

4.2 Experimental Methods

This work considered three different variables. The density ρ which changes the probability of detachment, the particle size R_p which changes the probability of collision and probability of detachment. The last variable is the volumetric flow rate, which changes the bubble radius and Reynolds number for the experiment set-up, which both change the probability of collision. The densities of molybdenum and iron are investigated. For molybdenum, several different particle sizes are tested as can be seen in table 4.1. These particle sizes are all tested for flow rates 5, 10, 25, 40, 50 and 70 sccm. For iron the particle sizes are also displayed in table 4.1 and these are tested for flow rates 10, 25, 40 and 50 sccm.

particle	Particle Size μm	density g/cm^3
Molybdenum Mo	5 10 88 100 149	10.22 [17]
Iron Fe	10 74 841	7.874 [29]

Table 4.1: particles used and their size

For every size of particle, approximately 0.2g is weighted and introduced in the separatory funnel with fluid. Meanwhile the airflow is started and the particles are introduced into the flotation column. The flotation products are collected after t= 10, 30 and 60 min. As can be seen in figure 4.2b not all flotation product was collected due to deposit at the glass of the set-up arch. After the t=60 min sample, this deposit is collected and added to the total extraction efficiency. Afterwards, the deposit at the bottom of the column and the leftover particles floating in the column are collected.

When collected, the samples are filtered with filtering paper with pass-through density smaller than 2.5μm for the particles with radius 5μm and with the density of 45μm for the other particles.

After filtering, the filters are put inside crucibles and put into a Venticell Eco Line to dry the filters. When dry, the filters are burned inside the Borel oven which heats up to 550°C. This temperature is chosen to make sure all of the filter is burned. The filters start burning at a lower temperature already, but by setting the max temperature to 550°Cit is made sure the filters are at least several hours exposed to a temperature above the burning temperature.

After burning the filters, the crucibles are weighted. The final weight of the particles has to be corrected because when being exposed to air molybdenum and iron react with oxygen in the following way:

$$2Mo + 3O_2 \rightarrow 2MoO_3 \tag{4.1}$$

$$3Fe + 2O_2 \rightarrow Fe_3O_4 \tag{4.2}$$

The eventual correction is depending on relative concentration of Mo and MoO_3 and of Fe and Fe_3O_4. These relative concentrations are determined by a X-ray Powder Diffraction scan. The correction factors are given by:

$$\frac{MM\ Mo}{0.12MM\ Mo + 0.88MM\ MoO_3} = 0.6943 \tag{4.3}$$

$$\frac{MM\ Fe}{MM\ Fe_3O_4} = 0.3497 \tag{4.4}$$

Hence, the total weight of the particles found has to be multiplied by the factor above to get the real weight of the extracted particles molybdenum and iron

The liquid used to represent the Molten Salt is a water-glycerol mixture with properties diplayed in 4.2. The water-glycerol mixture with ratio $41.5 mass - \%$ which has almost the same kinematic viscosity as the fluid inside the molten salt reactor. Therefore the fluid used during the experiment and the molten salt have a comparable Reynolds number.

Name	Density g/cm^3	Kinematic viscosity mm^2/s
Water	0.998	1.004
Glycerol	1.260	1.189
Water-Glycerol 41.5 $mass\%$	1.107	3.999

Table 4.2: properties water and glycerol whom together model as the molten salt at a temperatur of 293 K [30]

4.3 Model

The removal rate is determined by a time function given by:

$$\frac{dC}{dt} = k(C_2 - C_1) \tag{4.5}$$

where k is the flotation rate constant and C is the particle concentration in mass per unit volume . Assuming the first-order rate equation [21], the extraction rate can be calculated as follows:

$$E = E_{max}\left[1 - e^{-k \cdot t}\right] \tag{4.6}$$

To obtain the variables E_{max} and k cftool matlab is used. the flotation rate constant k is found by fitting a line with equation described in 4.6 through the extractions on t=10, 30 and 60 min. this can be seen in figure 4.3a. Next a line with equation 4.6 and a found value k is fitted through the total extraction rate as displayed in figure 4.3b.

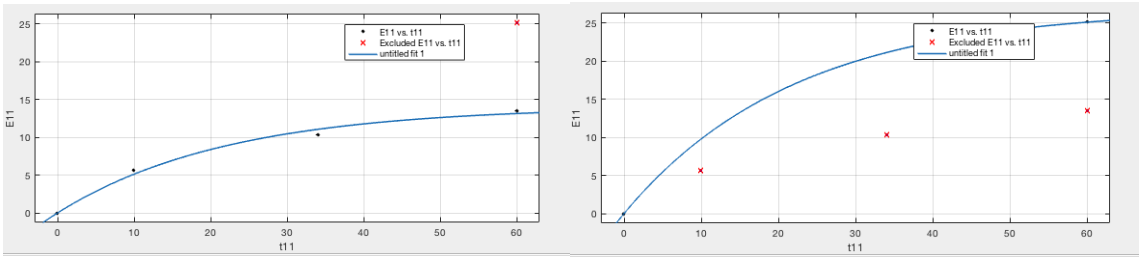

(a) Fit through time dependent points t=10, 30 and 60 min.

(b) time dependent fit through maximal extractin efficiency point

Figure 4.3: Fit with equation 4.6 through the time dependent points (a), Fit with the time dependent coefficient k through the point of maximal extraction efficiency (b)

4.4 Neutron Flux

To validate the matlab script used, different data is used to compare the prediction from the model and some real values. The data provided is the data of the neutron flux inside a reactor depending on how much two fuel rods are inserted into the reactor. The distance that the rods are inserted varies from 0 (not inserted) to 1 (totally inserted).

First the RBF is trained for optimal c. With the optimal c, Leave One Out (LOO) is done on 10 random points. LOO training is a way of training a model where all datapoints are used except one. By doing this, the use of data to train on is maximised. Therefore a model can be trained for small datasets which decreases the amount of time necessary for doing experiments. Before the LOO validation is done, the data is truncated. An allowed error of 10^{-5} % between the original and truncated data set is defined. For this small error, the data set can already be truncated from 196 to 12 modes. The rapid decrease in error can be seen in figure 4.4a. The result of the Radial Basis Function optimisation is displayed in figure 4.4b. An average error of 3.4% is achieved from LOO training 10 randomly chosen points.

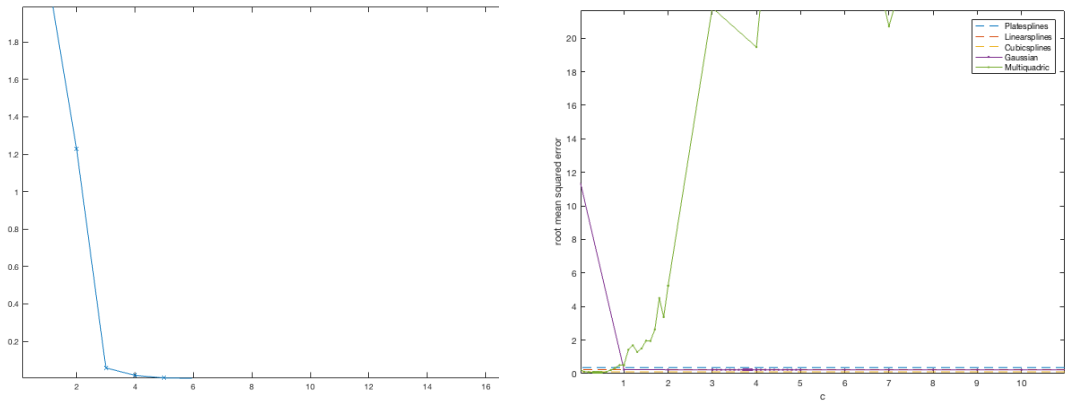

(a) Error with number of modes left over on the x-axis.

(b) RBF optimisation for the neutron flux inside a reactor.

Figure 4.4: Truncation error in figure (a) and the RBF optimisation in (b) with optimal c=3.84

Chapter 5

Results

5.1 Iron

To make a model for the extraction rate of iron, a RBF optimisation is done on the time dependent extraction rate displayed in figure 5.1a and total extraction efficiency is displayed in table 5.1. The RBF optimisation is shown in figure 5.1b. For the data on iron an optimal RBF is found for the Gaussian kernel function with c=4.36.

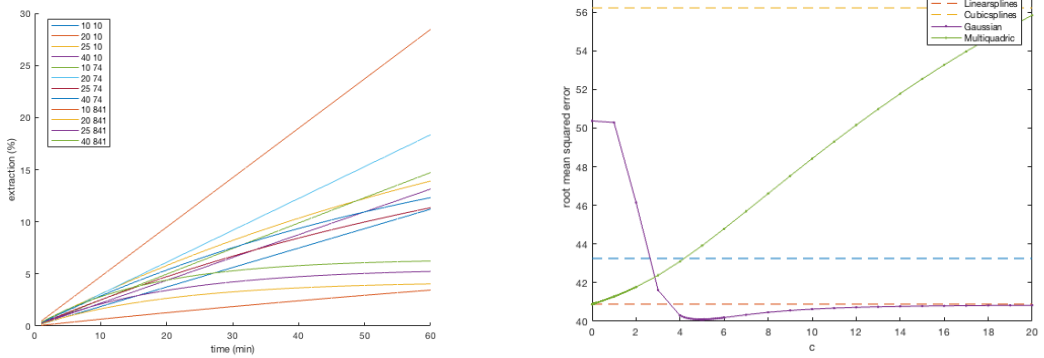

(a) Time dependence of Iron particles with in the legend the first number as $\dot{V}$ and the second number the particle size

(b) RBF optimisation of the time dependent data of iron

Figure 5.1: time-dependent extraction rate of iron (a) and the RBF optimisation which gives c=4.36 as optimal value (b)

Table 5.1: extraction efficiency of iron (%)

particle size $\mu m \downarrow$ flow sccm $\rightarrow$	10	20	25	40
10	11	28	14	13
74	15	18	11	12
841	3	4	5	6

To test the ability of this RBF with optimised c to make an approximation of the time dependency of the extraction, LOO training is used. This can only be done for $\dot{V}$ 20 and 25 from R=74 because these are the only non-limit values. If one would try this for other

variables the RBF would have to extrapolate, which is not the aim of the RBF. The results are shown figure 5.2. The corresponding L2-norms are respectively 29% and 37%. For the total extraction, also LOO is applied. Again only for $\dot{V}$ 20 and 25 from particle 74 an approximation can be made. The outcome of the approximated extraction efficiency are 12% and 17% respectively. The relative L2-norm of these results are 32% and 48%. The L2-norm is also known as the Euclidean distance and depicts the error of the approximation.

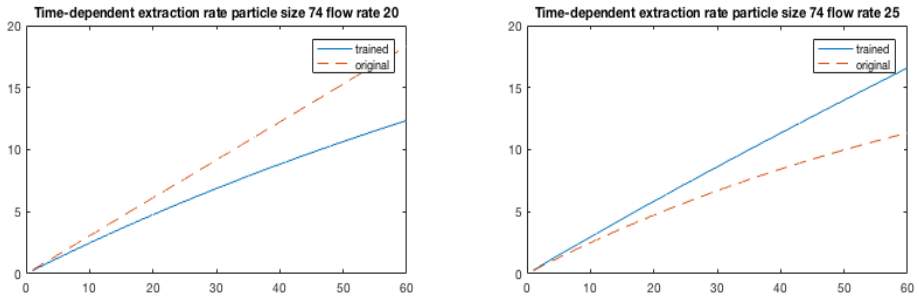

Figure 5.2: Approximation of the time dependent extraction efficiency calculated with the Gaussian Radial Basis Function with c=6.32

Conclusion

From the high L2-norm it can be concluded that the model is not sufficient for predicting the extraction rate of iron. Especially the fact that the wrong filter was used for the particle sizes R=10 decreases the model to train on, from the mere 12 reliable points to 8 points. These 8 points alone would not suffice as a training set because this would only include 2 points on the particle size grid. This is not enough to do LOO training and therefore the unreliable measurements from particle size 10 are included. These measurement nevertheless, form a poor basis to train a model on. Furthermore, the particle size grid is too irregularly distributed. The step from 74 to 841 is too big to make a good approximation in the range around either of both particle sizes. From figure 5.1a can be seen that there is almost no time dependency as expected. This can be derived from the straight lines instead of the exponential dependency we expect from equation 4.6. From this amount of data it is unclear to conclude if this low time-dependence is due to an error in the measurements or if iron does not have a high time dependence.

5.2 Molybdenum

For molybdenum, the time dependent extraction is displayed in figure 5.3 and total extraction efficiency is shown in table 5.2.

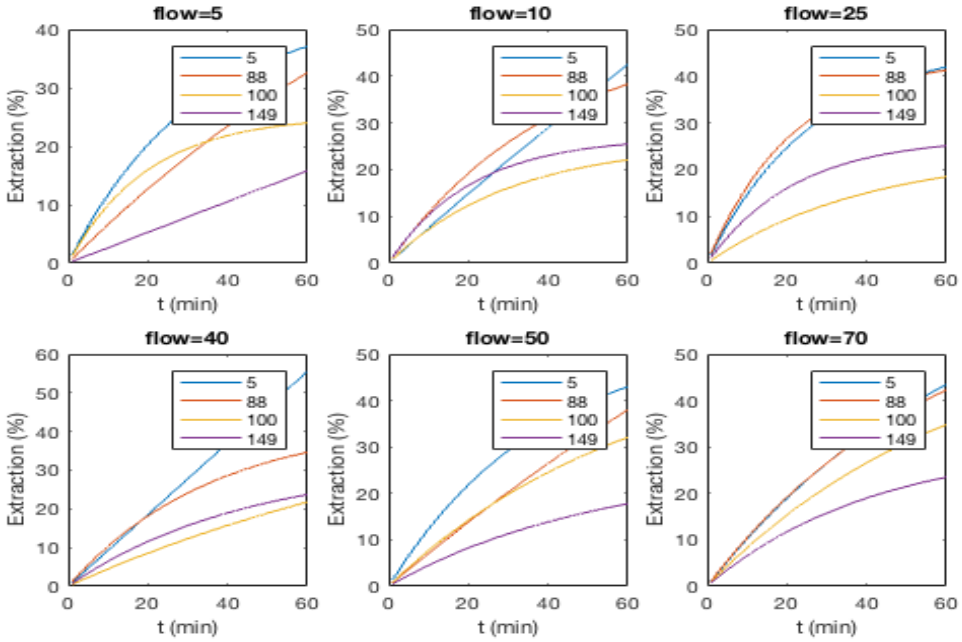

Figure 5.3: Time dependence of molybdenum per volumetric flow rate $\dot{V}$ and all different particle sizes R

Table 5.2: extraction efficiency of molybdenum (%). *experiment conducted by dr. E. Capelli

particle size $\mu m \downarrow$ flow sccm $\rightarrow$	5	10	25	40	50	70
5	37	43	42	56	43	43
88	33*	38	41*	35	38*	42
100	24	22	18	22	32	35
149	16*	25	25*	24	18	23

Again, an analysis of the RBF is done for Molybdenum. The results for the optimisation for both the time dependent extraction rate and final extraction for the uncorrected data are displayed in Figure 5.4. The optimal value is c=6.57.

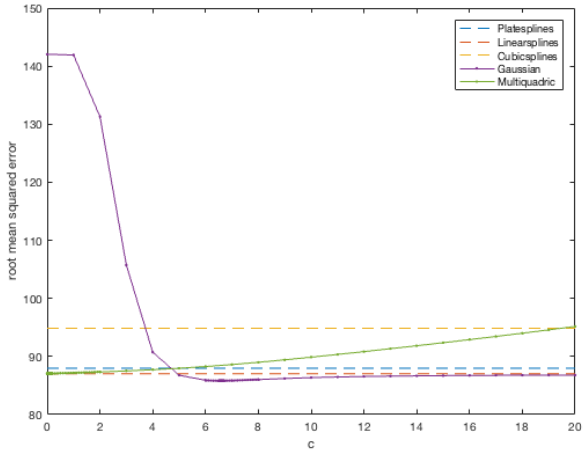

Figure 5.4: c-optimisation for the total extraction and time dependent data of Molybdenum

With these RBF's, LOO training can be done for particle sizes 88 and 100 μm with volumetrci flow rate $\dot{V}$ 10, 25, 40 and 50 sccm. The results of the time dependent approximations are presented in figure 5.5. The L2 norm corresponding to the approximated time dependence is shown in table 5.3 For the total extraction efficiency LOO predicts the extractions shown in table 5.4. Euclidean distances corresponding with these predictions are shown in table 5.5.

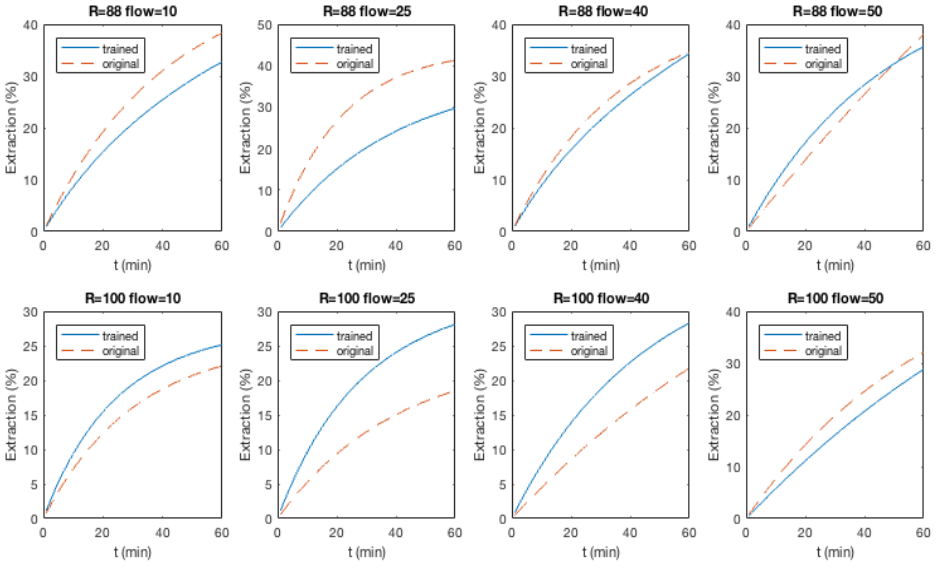

Figure 5.5: approximation made with leave one out training of Molybdenum

Conclusion

The experiments for particle sizes 88 and 149 for $\dot{V}$ 5 and 10 only consist of two samples (three if t=0 is included), which result in an irregular time dependency. This causes an error when using data points to train on. Furthermore the $\dot{V}$ 10 and 40 of particle size 5

Table 5.3: relative L2-norm of the time dependent extraction efficiency approximation (%)

particle size $\mu m \downarrow$ flow sccm $\rightarrow$	10	25	40	50
88	17	35	8	10
100	18	61	43	15

Table 5.4: extraction efficiency approximation (%)

particle size $\mu m \downarrow$ flow sccm $\rightarrow$	10	25	40	50
88	33	30	34	36
100	25	28	28	29

Table 5.5: relative error extraction rate approximation (%)

particle size $\mu m \downarrow$ flow sccm $\rightarrow$	10	25	40	50
88	14	28	1	6
100	14	52	30	10

are straight lines which suggests that they do not have an exponential time dependence. For $\dot{V}$ 10 this can be explained by the fact that these samples are filtered with a filter with pore size bigger than 5 μm and therefore not all extracted particles are collected. The $\dot{V}$ 40 experiment was conducted with the right filter, so the straight line indicates an error in the measurement. It is unclear how the high error on $\dot{V}$ 25 particle size 100 is caused. Therefore it is assumed it is a result of an experimental error.

5.2.1 Correction

The experiments have big differences in the total percentage of particles recovered after the experiment. To make sure the approximation is not influenced by an error due to missing particles, the total extraction is corrected to make every total recovery of particles 100%. However, this correction only increases the error as can be seen in table 5.6 and therefore this correction is not used for further analysis. The loss of particles could partially be explained by the fact that the correction factor from equation 4.3 and 4.4 are not adjusted for different experiments. Some experiments may have had a longer heating cycle which causes more oxidation. Therefore their actual weight might be different than considered.

Table 5.6: Relative error extraction efficiency approximation from corrected data (%)

particle size $\mu m \downarrow$ flow sccm $\rightarrow$	10	25	40	50
88	7	37	16	10
100	24	54	25	16

5.2.2 Compensation Measurement Errors

In table 5.7 the flotation rate constants of molybdenum are shown. It can be seen that some of the results are not in line with its neighbours. In this subsection, an attempt is made to improve the data on physical and emperical motives.

Table 5.7: Time coefficient k from equation 4.6

particle size $\mu m \downarrow$ flow sccm $\rightarrow$	5	10	25	40	50	70
5	0.031	0.0024	0.037	3.5e-04	0.025	0.015
88	0.0082	0.024	0.047	0.028	0.0045	0.017
100	0.050	0.033	0.025	0.0087	0.016	0.016
149	2.1e-05	0.048	0.045	0.022	0.019	0.023

It becomes clear that for $\dot{V}$ 5 sccm particle size 149 μm and for $\dot{V}$ 40 sccm particle size 5 μm the flotation rate constants are divergent from the neighbouring ones. For the experiment with $\dot{V}$ 5 sccm particle size 149 μm this deviation can be dedicated to the fact that the experiment for this point only consisted of 3 time points instead of 5. Therefore the fit becomes an almost straight line with time-dependence coefficient $k \ll 1$.
For the experiment with $\dot{V}$ 40 sccm and particle size 5 μm there is no clear explanation for the deviation in value of the flotation rate constant. The difference could be explained by the different sample sizes taken. Because the particles have a small radius they do not directly precipitate. Thus not all particles extracted deposit at the bottom of the extraction reservoir. Therefore the number of particles taken is highly dependent of the size of the sample taken. If the first samples are too small and the sample on t=60 too big, the flotation rate constant becomes zero and the extraction rate becomes a straight line.

To see how much error these two experiment cause while training on them, new flotation rate constants are predicted by extrapolation. The suggested flotation rate constants can be found in table 5.8. The new LOO trained time dependent extraction efficiency is displayed in figure 5.6. The error corresponding to the new approximation can be found in table 5.9. The extraction efficiency does not change for different flotation rate constants and can still be found in table 5.2.

Table 5.8: Suggested time coefficients k from equation 4.6

particle size $\mu m \downarrow$ flow sccm $\rightarrow$	5	10	25	40	50	70
5	0.031	0.0024	0.037	0.033	0.025	0.015
88	0.0082	0.024	0.047	0.028	0.0045	0.017
100	0.050	0.033	0.025	0.0087	0.016	0.016
149	0.054	0.048	0.045	0.022	0.019	0.023

Table 5.9: the relative L2-norm of the time dependent extraction of the compensated data (%)

particle size $\mu m \downarrow$ flow sccm $\rightarrow$	10	25	40	50
88	17	34	7	11
100	18	60	42	15

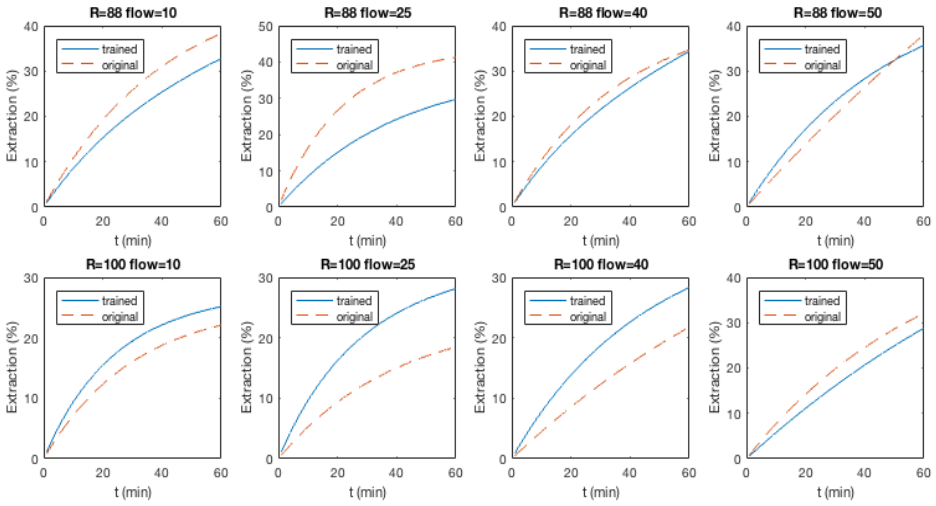

Figure 5.6: approximation made with leave one out training of the manipulated data.

Conclusion

From the error found in table 5.9 it can be concluded that the two bad flotation rate constants do not influence the rest of the data much. However it is likely the constants were wrong and new measurements are therefore required.

5.2.3 Validation

To validate the used model some off-grid point will be approximated by the model and tested with experimental data of this input. The point with volumetric flow rate $\dot{V}$ 15 sccm and particle size 30 μm is tested.

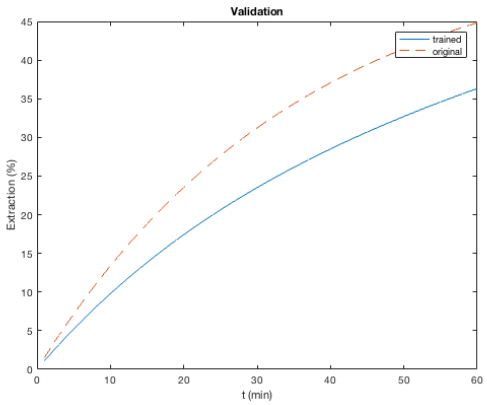

Figure 5.7: validation for the point R=30 $\dot{V}$=15 trained on the original data

In figure 5.7 the predicted outcome of the time dependent extraction efficiency and the measured data can be seen. The total L2-norm for the time dependence is 24%. The total expected extraction is 36 and has an relative L2-norm of 21%.

Conclusion

From this validation experiment it can be concluded that the model could work. The error of 24% and 21% could be reduced if there is more data.

5.2.4 RBF versus Interpolation

Radial Basis Functions are particularly good in modelling complex systems with several variables. Because our system has only got two variables it may seem redundant to use a RBF. The RBF uses more computer power and it would therefore be favourable if an interpolation would suffice. The results of an interpolation for the total extraction are shown in table 5.10 and its error in table 5.11

Table 5.10: relative error extraction rate approximation with RBF (%)

particle size $\mu m \downarrow$ flow sccm $\rightarrow$	10	25	40	50
88	14	28	1	6
100	14	52	30	10

Table 5.11: relative error extraction rate approximation with interpolation (%)

particle size $\mu m \downarrow$ flow sccm $\rightarrow$	10	25	40	50
88	36	39	17	23
100	45	85	64	8

Conclusion

From the results of the interpolation we can conclude that the Radial basis function is a better way to model the data than an interpolation.

Chapter 6

Conclusion

The approximation of the extraction efficiency for iron is not sufficient. This is due to the low amount of reliable data available, which causes errors of 29% and 37%. For molybdenum more data was available which reduced some errors to only 8%. Though, some experiments still had a relative error as high as 61%. By correcting the data these errors did not improve. The model does not improve drastically when compensating irregular results. However from physical and empirical point of view, the measurements were wrong and new measurements are therefore required. The validation test showed a 21% error in extraction efficiency and 24% in the time dependent approximation.

The used method provided measurements with much deviation. The method should be improved for further use in a follow-up study. The set-up needs to be improved to make the sample size constant. Furthermore, more experiments need to point out if the measurement errors can be prevented.

The model itself has proven to be appropriate during the approximation of the neutron flux. For molybdenum the model also performed better on RBF than on interpolation. Unfortunately there are not enough data points to give a very precise prediction and the influence of the particle density is not included in the model yet.

Chapter 7

Recommendation

To lower the error in time-coefficient, a second valve could be introduced after the current valve of the Hallimond tube. By placing a second valve, a constant volume can be introduced between the two valves. If all samples are the same size, it is less likely to underestimate or overestimate the time-coefficient.

Moreover from the results it becomes clear that extra measurements have to be done to improve the model. To improve the range of particles sizes, experiments with radii outside the current particle size domain should be done. To improve the accuracy different particle sizes inside this domain should be included.

Furthermore to get the desired model which is also trained for different particle densities, several types of particles need to be examined in the same particle size R and volumetric flow rate $\dot{V}$ domain as iron and molybdenum. An evenly distributed grid for volumetric flow rate, particle size and particle density are desired to improve the accuracy.

Bibliography

[1] D.J. Journee. Helium bubbling in a molten salt fast reactor. *Delft: TU delft*, pages 7–12, 29–30, 57, 2014.

[2] L. Doman. EIA projects 28 % increase in world energy use by 2040, 2017.

[3] R Alvarez. Thorium: the wonder fuel that wasnt. *Bulletin of the Atomic Scientists*, (7), 2014.

[4] Thorium. *World Nuclear Association*, 2017.

[5] The thorium fuel cycle. *Australian Nuclear Science and Technology Organisation*, 2013.

[6] D Yurman. India Commits to Fast Reactor Fuel Cycle Facility for U-233, 2017.

[7] D Mathers. The thorium fuel cycles. *ThEC2013 presentation*, (7), 2013.

[8] F Arkin. An alternative fuel for nuclear energy looms, 2016.

[9] A. Gurria. Introduction of thorium in the nuclear fuel cycles, short- to long-term considerations. *NEA No. 7224, OECD 2015*, pages 99 – 100, 2015.

[10] S.Williams. How Molten Salt Reactors Might Spell a Nuclear Energy Revolution, 2017.

[11] C. Forsberg. *Molten-Salt-Reactor Technology Gaps*, volume paper 6295. 2006.

[12] J. Kloosterman O. Benes S. Delpech etc. J. Serp, M. Allibert. The molten salt reactor in generation iv: Overview and perspectives. *Elsevier, Progress in Nuclear Energy*, 77:308–319, 2014.

[13] M. Elsheikh. Safety assessment of molten salt reactors in comparison with light water reactors. *Journal of Radiation Research and Applied Sciences*, 6(2):63 – 70, 2013.

[14] C.J.L. Lock P.C. Davidge. Neutron poison by gaseous fission products. *Journal of Nuclear Energy (1954)*, 6(3):191 – 196, 1958.

[15] G. J. Schrobilgen. Krypton. *Encyclopaedia Britannica, inc.*, 2018.

[16] G. J. Schrobilgen. Xenon. *Encyclopaedia Britannica, inc.*, 2018.

[17] L. Gonzlez J. A. Pero-Sanz Elorz, M. Hernndez. *Chapter 1 - Solidification of Metals,*. Elsevier, 2017.

[18] Pubchem compound database; cid=23957. *National Center for Biotechnology Information*, 2018.

[19] S Cantor. Density and viscosity of several molten fluoride mixtures. 03 1973.

[20] A. Singh R. Prakash, S. Majumder. Flotation technique: Its mechanisms and design parameters. *Chemical Engineering and Processing - Process Intensification*, 127:249 – 270, 2018.

[21] B. Hassas A. Eskanlou, B. Shahbazi. Estimation of flotation rate constant and collision efficiency using regression and artificial neural networks. *Separation Science and Technology*, page 374388, 2017.

[22] Rezai B Chelgani S, Shahbazi B. Estimation of froth flotation recovery and collision probability based on operational parameters using an artificial neural network. *International Journal of Minerals, Metallurgy and Materials*, 17:526–534, 2010.

[23] H. J. Schulze. Flotation as a heterocoagulation process: Possibilities of calculating the probability of flotation. *Coagulation and Flocculation*, pages 321–353, 1993. Cited By :53.

[24] R.H. Yoon. The role of hydrodynamic and surface forces in bubbleparticle interaction. *InternationalJournal of Mineral Processing*, 58(1):129–143, 2000.

[25] V.e. Ross. Particle-bubble attachment in flotation froths. *Minerals Engineering*, 10(7):695706, 1997.

[26] H. Schulze. *Physico-chemical Elementary Processes in Flotation, An Analysis from the Point of View of Colloid Science including Process Engineering Considerations*. Elsevier, 1984.

[27] R Ralston. Bubbleparticle attachment and detachment in flotation. *InternationalJournal of Mineral Processing*, 56):133–164, 1999.

[28] V. Buljak. *Inverse ananysis with model reduction*. Springer, 2012.

[29] Iron. *Encyclopaedia Britannica, inc.*, 2018.

[30] M. Warmoeskerken L.Janssen. *Transport Phenomena Data Companion*. VSSD, 2006.